

Surface displacement of the Mw 7 Machaze earthquake (Mozambique): Complementary use of multiband InSAR and radar amplitude image correlation with elastic modelling.

Daniel Raucoules, B. Ristori, Marcello de Michele, P. Briole

► **To cite this version:**

Daniel Raucoules, B. Ristori, Marcello de Michele, P. Briole. Surface displacement of the Mw 7 Machaze earthquake (Mozambique): Complementary use of multiband InSAR and radar amplitude image correlation with elastic modelling.. *Remote Sensing of Environment*, Elsevier, 2010, 114 (10), pp.2211-2218. 10.1016/j.rse.2010.04.023 . hal-00509818v2

HAL Id: hal-00509818

<https://hal-brgm.archives-ouvertes.fr/hal-00509818v2>

Submitted on 28 Jun 2011

HAL is a multi-disciplinary open access archive for the deposit and dissemination of scientific research documents, whether they are published or not. The documents may come from teaching and research institutions in France or abroad, or from public or private research centers.

L'archive ouverte pluridisciplinaire **HAL**, est destinée au dépôt et à la diffusion de documents scientifiques de niveau recherche, publiés ou non, émanant des établissements d'enseignement et de recherche français ou étrangers, des laboratoires publics ou privés.

1 **Surface displacement of the M_w 7 Machaze earthquake (Mozambique): Complementary use of**
2 **multiband InSAR and radar amplitude image correlation with elastic modelling.**

3

4

5 Raucoules D. (1), Ristori B. (1), de Michele M. (1), Briole P. (2)

6

7 (1) BRGM 3 avenue Claude Guillemin 45060 Orléans cedex 2 France

8 Corresponding author: d.raucoules@brgm.fr

9 (2) ENS, Laboratoire de Géologie, 24 Rue Lhomond, 75005 Paris

10

11

12 **Abstract**

13

14 In this paper we investigate the surface displacement related to the 2006 Machaze earthquake using
15 Synthetic Aperture Radar Interferometry (InSAR) and sub-pixel correlation (SPC) of radar amplitude images.
16 We focus on surface displacement measurement during three stages of the seismic cycle. First, we
17 examined the co-seismic stage, using an Advanced SAR (ASAR) sensor onboard the Envisat satellite. Then
18 we investigated the post-seismic stage using the Phase Array L-band SAR sensor (PALSAR) onboard the
19 ALOS satellite. Lastly, we focussed on the inter-seismic stage, prior to the earthquake by analysing the L-
20 band JERS-1 SAR data. The high degree of signal decorrelation in the C-band co-seismic interferogram
21 hinders a correct positioning of the surface rupture and correct phase unwrapping. The post-seismic L-band
22 interferograms reveal a time-constant surface displacement, causing subsidence of the surface at a ~ 5
23 cm/yr rate. This phenomenon continued to affect the close rupture field for at least two years following the
24 earthquake and intrinsically reveals a candidate seismogenic fault trace that we use as a proxy for an
25 inversion against an elastic dislocation model. Prior to the earthquake, the JERS interferograms do not
26 indicate any traces of pre-seismic slip on the sismogenic fault. Therefore, slip after the earthquake is post-
27 seismic, and it was triggered by the Machaze earthquake. This feature represents a prominent post-seismic
28 slip event rarely observed in such a geodynamic context.

29

30

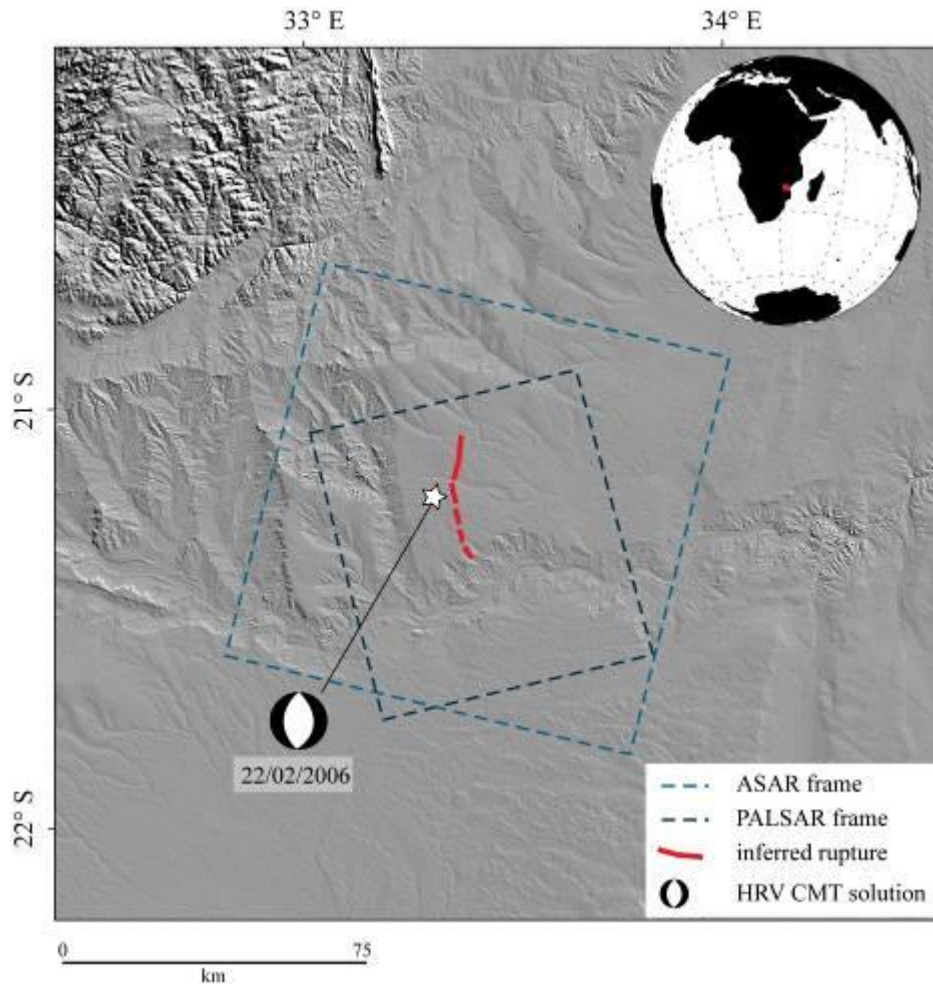
31 **1 Introduction**

32

33 On February 22, 2006, a M_w 7.0 earthquake occurred in Machaze, Manica Province, Mozambique (Figure 1)
34 affecting an area characterised by low-level historical seismicity. This earthquake inflicted little damage on
35 property and individuals, mainly because of the typology and density of housing in the area (i.e. scattered
36 villages with light-weight structures). During the 20th century, three earthquakes with magnitudes larger than
37 5.0 concerned this area: the first in 1951 and the two others in 1957. They were characterised by shallow
38 slip at depths of less than 20 km (Fenton & Bommer, 2006). The fault system associated with these
39 earthquakes can be related to the southern portion of the East African Rift and belongs to a divergent plate-
40 boundary geodynamic context. The 2006 Machaze earthquake occurred at a depth of 12 km and produced a
41 north-south oriented surface rupture about 30-40 km long with a co-seismic surface slip of up to 2 metres
42 (Fenton & Bommer, 2006). The fault ruptured with a normal mechanism with a 70° west dipping fault plane.
43 Fenton & Bommer (2006) stated that the surface rupture, although visible in the field, could not be followed
44 along its entire length due to the danger posed by buried land mines in the area. Moreover, extensive
45 liquefaction phenomena were associated to this event (Lopez-Querol et al., 2007).

46 In this paper, we called on remote-sensing satellite data to complement data acquired on the ground to help
47 understand the Machaze earthquake. In particular, we used InSAR (e.g. Massonnet & Feigl, 1998) and SPC
48 (e.g. Michel & Avouac, 2002) techniques along with Envisat-ASAR, JERS-1 and ALOS-PALSAR data to
49 measure the ground surface displacement produced by the Machaze earthquake at different stages of the
50 seismic cycle, i.e. before, during and after the earthquake. Then, we used the co-seismic displacement field
51 to constrain the seismogenic fault geometry at depth by inverting the surface displacement field against a
52 simple elastic dislocation model (Briole et al., 1986).

53 We proceeded as follow. First, we used the ALOS PALSAR data to produce a post-seismic interferogram
54 revealing the position and surface geometry of the seismogenic fault (not observable on the co-seismic
55 interferograms because of high deformation rates). Then we looked at the inter-seismic interferograms to
56 detect possible creep or pre-seismic slip on this previously unmapped fault. Finally, we built a co-seismic
57 interferogram and used the retrieved fault surface geometry parameters to constrain the fault's co-seismic
58 slip and geometry at depth by means of an inversion procedure.



59

60

61 Figure 1 : Location of the Machaze Earthquake

62

63 2 Data

64

65 In this study, we made a complementary use of C and L band radar from different sensors. Due to the dense
 66 vegetation covering the terrain in the area of interest and the large size of surface deformation expected (~
 67 metre), we decided to use ALOS-PALSAR and JERS-1 L-band radar data. Moreover, the measurements
 68 obtained from radar data at longer wavelengths (23 cm as opposed to 5.6 cm for C-band) would be less
 69 affected by fringe aliasing as there would be fewer fringes for given deformation values. Therefore,
 70 interferometric phases could be unwrapped over larger areas (e.g. Raucoules et al., 2007). Unfortunately,
 71 ALOS and JERS-1 data were not available during the co-seismic phase of the Machaze earthquake. We
 72 accordingly called on Envisat/ASAR C-band data to retrieve co-seismic surface displacement while using

73 ALOS-PALSAR and JERS-1 to investigate possible post-seismic and pre-seismic surface displacement
74 respectively. In this study we used six PALSAR images (Dec. 2006- Dec. 2008, ascending mode), seven
75 ASAR images (Nov. 2003, Feb. 2007, descending mode) and three JERS-1 images (Apr. 1993 – Oct. 1996,
76 ascending mode). Tables 1 to 3 describe the characteristics of the PALSAR, ASAR and JERS-1
77 interferograms that we built using the GAMMA software (Wegmuller et al., 1998).

78

79 Table 1: Interferograms produced using ALOS PALSAR SAR images. Post-seismic period.

80

Interferogram	Image1 (date)	Image2 (date)	<i>Perpendicular baseline (m)</i>	<i>Time span (days)</i>
1	20061226	20070210	725	46
2	20061226	20071229	-881	368
3	20061226	20080213	-632	414
4	20061226	20080330	-1191	460
5	20061226	20081231	1512	736
6	20070210	20071229	-1607	322
7	20070210	20080213	-1357	368
8	20070210	20080330	-1916	414
9	20070210	20081231	787	690
10	20071229	20080213	249	46
12	20071229	20081231	2394	368
13	20080213	20080330	-558	46
14	20080213	20081231	2145	322
15	20080330	20081231	2704	276

81

82

83 Table 2: Interferograms produced using ASAR Envisat SAR images. Co-seismic period.

84

<i>Interferogram</i>	<i>Image1</i>	<i>Image2</i>	<i>Perpendicular baseline (m)</i>	<i>Time span (days)</i>
1	20031109	20060507	720	910
2	20031109	20060611	230	945
3	20031109	20070211	432	1190
4	20040118	20060507	1114	840
5	20040118	20060611	623	875
6	20040118	20070211	826	1120
7	20040328	20060507	-131	770
8	20040328	20060611	-622	805
9	20040328	20070211	-420	1050
10	20040606	20060507	-198	700
11	20040606	20060611	-689	735
12	20040606	20070211	-486	980

85

86

87 Table 3: Interferograms produced using JER-1 SAR images. Pre-seismic period.

88

<i>Interferogram</i>	<i>Image1</i>	<i>Image2</i>	<i>Perpendicular baseline (m)</i>	<i>Time span (days)</i>
1	19930406	19950311	-68	704
2	19930406	19960820	110	1232
3	19950311	19960820	179	528

89

90

91

92 **3 Data Processing**

93

94 *Post-seismic Slip*

95

96 For each of the three observation periods, we apply different processing strategies.

97 - Hashimoto et al. (2007) detected and provided a preliminary estimate of the post-seismic deformation

98 phenomenon based on a single ALOS/PALSAR pair prior to December 2006. Our objective here has

99 therefore been to obtain a precise location of the displacement field and to derive the post-seismic

100 displacement rate over a longer period. We further would be interested in ascertaining whether post seismic

101 displacement is decelerating. In this perspective, we built a stack of 15 unwrapped interferograms according

102 to the methodology proposed by Le Mouelic et al. (2005):

103 [eq 1]
$$V = \frac{\langle \Delta\Phi \rangle \frac{\lambda}{2}}{\langle \Delta T \rangle 2\pi}$$

104 Brackets in eq. 1 indicate the average value on the data set. $\Delta\Phi$ is the interferometric phase, ΔT is the time

105 span associated with an interferogram and λ is the wavelength.

106 Under such conditions, averaging a series of interferograms reduces the relative importance of the

107 atmospheric component of the interferometric phase as compared with the displacement signal. Considering

108 the characteristics of the studied phenomenon (slow deformation with respect to the sensor wavelength) and

109 the good coherence of the interferograms, unwrapping errors will be reduced and should not impact the

110 velocity map.

111 Then, based on an optimization procedure, we estimated the velocity by linear regression (Gamma, 2008).

112 The result of this procedure was observed to be equivalent to that obtained by averaging. However, the

113 linear regression procedure allows an image to be achieved of the discrepancy with respect to the linear

114 regression (standard deviation) which provides quality control for the velocity estimation (in particular

115 including temporal fluctuation due to atmospheric effects), and useful information to identify possible non-

116 linear-with-time slip evolution during the observation period. The process accordingly yields a displacement

117 rate map and a map showing discrepancy with respect to linearity (Figures 2a, 2b).

118

119

120

121 *Inter-seismic Slip*

122

123 - Our objective for the pre-seismic period was to detect pre-seismic deformation. We therefore constructed
124 interferograms covering long time spans and examined them near the location of the earthquake rupture.
125 We should mention that the JERS-1 provides poor coverage for this study area (only three images
126 acquired).

127

128 *Co-seismic Slip*

129

130 - In order to map the co-seismic surface displacement, we built 12 differential interferograms. After visual
131 comparison of all the interferometric series produced (Table 2), we selected interferograms having the least
132 noise. In view of the high displacement rate (tens of interferometric fringes), the atmospheric component of
133 the interferometric phase is negligible with respect to the displacement component. The results are shown in
134 Figure 4.

135 As direct unwrapping is not relevant (areas with major deformation are not amenable because of the high
136 fringe rate), visible fringes were digitised manually in order to perform an inversion of a dislocation model
137 (Okada, 1985; Briole, 1986). Considering such a model as a direct source of information about the
138 phenomenon, we proposed to re-inject the inverted parameters so as to produce a simulated interferogram.
139 Once the simulated interferogram was subtracted from the initial interferogram, we obtained a residual,
140 which is easier to unwrap. The unwrapped residual was added to the simulated interferograms and provided
141 an improved unwrapped differential interferogram (Section 5).

142 It should be stated that the global unwrapping method used by Gamma tends to underestimate phase
143 gradient value where the residual image is noisy. The simulation can therefore help correct these errors. To
144 simplify the principle behind the proposed method, where the phase is noisy, the final result will correspond
145 to the model and where the initial interferogram signal is reliable, the result will correspond to the
146 interferometric data. In a certain way, this procedure interpolates the interferogram on the noisy areas (and
147 in particular in the near-field deformation area) by taking into account a physical model based on the far-field
148 deformation obtained by InSAR and ancillary knowledge about the earthquake.

149

150

151 **4 Results**

152

153 *Post-seismic Slip*

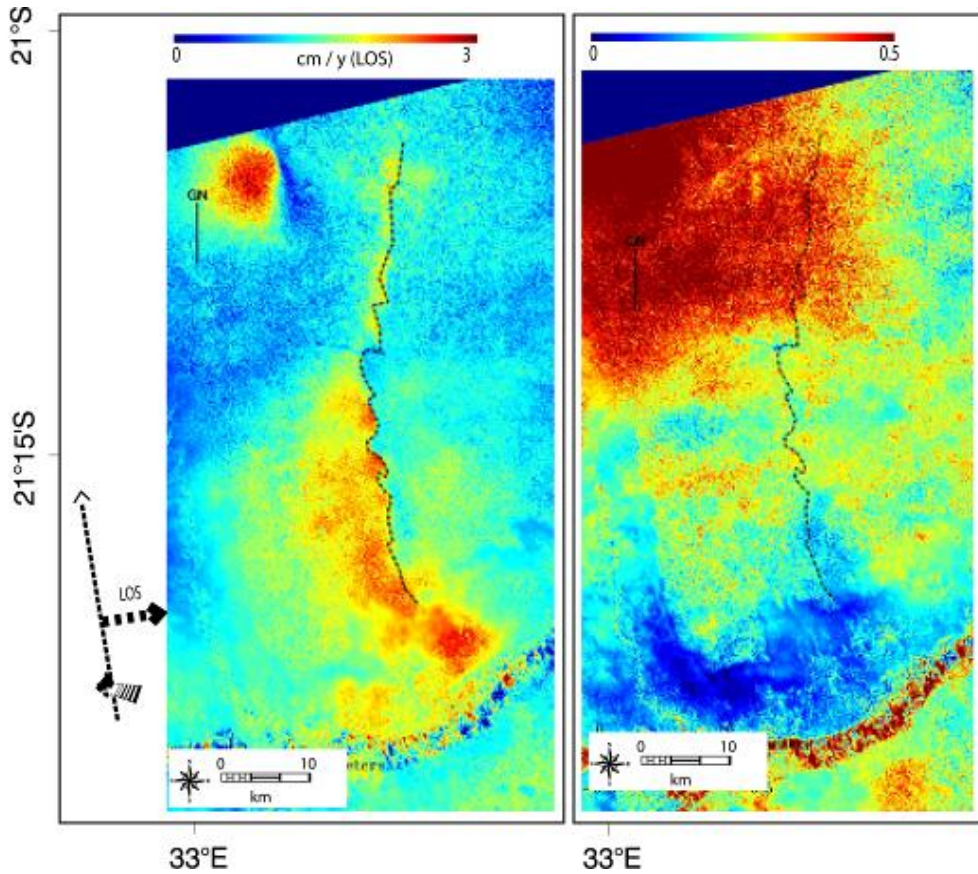
154

155 Figure 2a shows the displacement map derived from PALSAR interferometry. The most prominent feature in
156 the post-seismic displacement map is the constant-with-time subsidence affecting the area formerly
157 ruptured. The RMSE to linearity (Figure 2b) shows no correlation between the position of the rupture and the
158 discrepancy with respect to linearity. That suggests that surface displacement is characterised by a constant
159 rate over the 2-year observation period. In fact, the deformation along the rupture appears as linear as on
160 stable areas (where deformation is obviously linear), far from the rupture. We measured a post-seismic
161 surface displacement up to 3.5 cm/year, assuming a mainly vertical displacement phenomenon consistent
162 with a 70°-dip normal fault. This phenomenon affected the study area for at least two years after the
163 earthquake. According to our observations, post-seismic displacement did not decrease with time, though
164 this might be due to the relatively short window of observation. Assuming that the post-seismic displacement
165 occurred on the initial seismic rupture location, we can clearly locate (and digitise) a candidate for the co-
166 seismic surface rupture. At this stage of the processing, one might think that the seismogenic fault
167 underwent pre-seismic slip or creeping. We subsequently assessed the pre-seismic displacement field in the
168 near-fault field and tried to discriminate between post-seismic relaxations and a possible pre-seismic slip
169 component, which in principle should affect the area before the event as well.

170 Another prominent feature in the post-seismic displacement map is a 5 cm/yr vertical displacement feature
171 located NNW of Figure 2. At first sight, this phenomenon is difficult to correlate with the 2006 Machaze
172 earthquake as it is located 10 km west of the main rupture. Although not addressed in detail here, this
173 phenomenon certainly does merit further investigation.

174

175



176

177

178 Figure 2 a): Average deformation (2006-2008) in Line of sight (cm/year). The surface rupture (dashed line) has been
179 digitised on the image. b): RMSE (rad) of the re-ordered phase screens with respect to linear deformation (root-mean-
180 square residual to the estimated constant rate LOS displacement). No correlation with the rupture position is
181 observable.

182

183 *Pre-seismic Displacement*

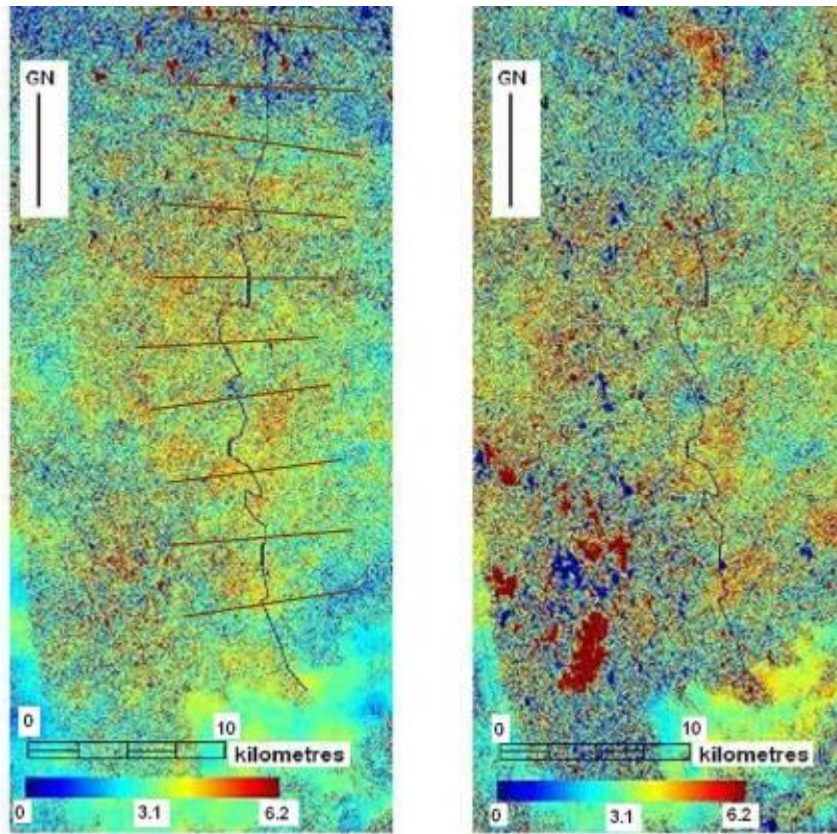
184

185 Figure 3 shows interferograms for the inter-seismic periods 1993-1995 and 1993-1996. No surface
186 displacement phenomena are identified in the vicinity of the seismogenic fault prior to the earthquake. This
187 observation leads us to rule out the presence of measurable pre-seismic slip or creep on this segment of the
188 fault.

189

190

191



192

193

194

195 Figure 3: a) 1993-1995 JERS-1 interferogram. Black line: the seismogenic fault trace derived from the post-seismic
196 displacement map. b) 1993-1996 JERS-1 interferogram. Values are given in radians. Positions of the ten 10-km profiles
197 used for offset computation (Table 4) have been plotted.

198

199 In order to confirm the observation, using a profile tool from the *cosi-corr* software (Leprince and Ayoub,
200 2007) designed to estimate deformation-value differences on either side of a fault by comparing linear
201 regressions, we derived the phase values. Table 4 presents the averages of estimations on ten profiles
202 (from north to south) perpendicular to the fault location.

203

204

205

206

207 Table 4: offset (in rad) on either side of the fault estimated from the interferograms for ten profiles. Sigma corresponds to
208 the standard deviations on the linear regressions on either side of the digitised fault computed by Cosi-corr.

209

<i>Interferogram 1993-1995</i>		<i>Interferogram 1993-1996</i>	
Offset (rad)	Sigma (rad)	Offset (rad)	Sigma (rad)
0.053	0.072	0.100	0.149

210

211

212 From Table 4 we can conclude:

213

214 - For the period 1993-1995, the mean deformation value equals approximately 0.05 rad (*i.e.* 0.09 cm), with a
215 mean sigma of 0.07 rad (*i.e.* 0.12 cm)

216 - For the period 1993-1996, the mean deformation value equals 0.10 rad (*i.e.* 0.2 cm), with a mean sigma of
217 0.15 (*i.e.* 0.3 cm)

218 The values obtained (about 1-3 mm) are very small in terms of the method sensitivity. There is accordingly
219 no pre-seismic motion on the fault that is high enough to be observed with conventional INSAR.

220

221 *Co-Seismic Deformation*

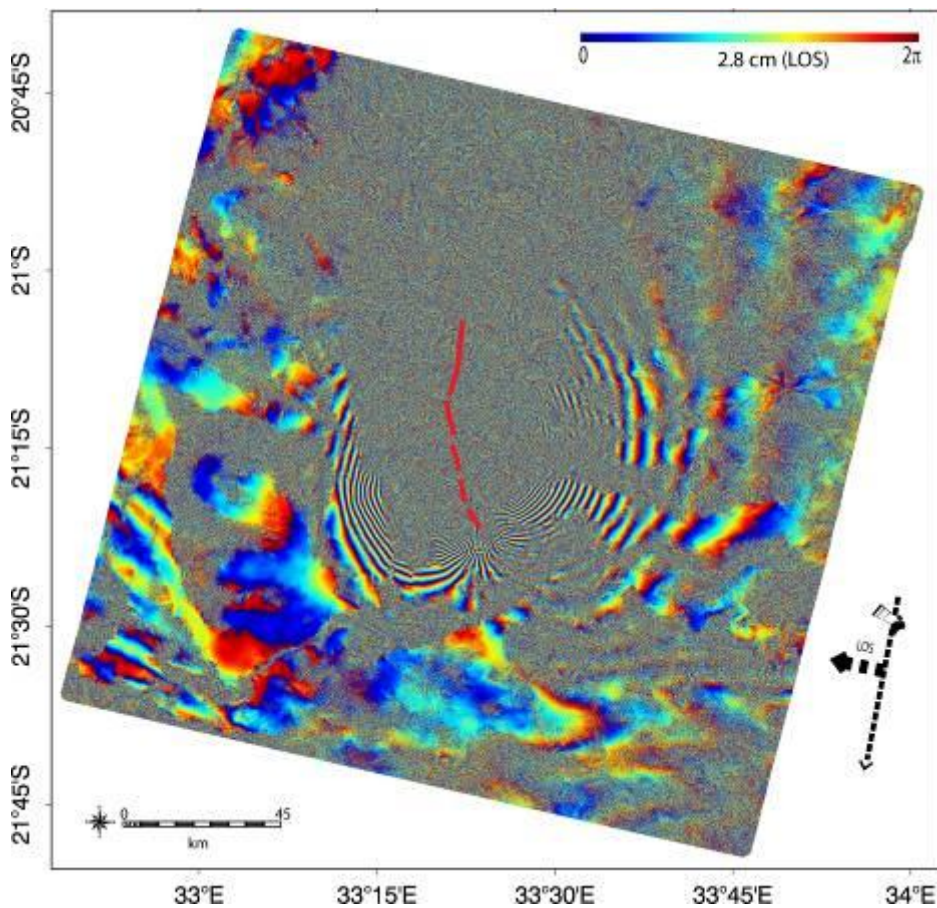
222

223 Interferogram 2004/04/06 – 2006/05/07 (Figure 4) was selected as the most relevant for interpretation in
224 terms of deformation. This interferogram provides information on the far-field deformation except on the
225 northern area where the coherence is poor (probably because of vegetation). We will note that the
226 deformation phenomenon observed in the post-seismic deformation map is located in the incoherent area.
227 We thus cannot confirm, based on this interferogram, that a rupture did indeed occur at this location.

228 The near-field deformation is, of course, not measurable because the deformation gradients (metres of
229 displacement on short distances) are far beyond what InSAR is capable of measuring.

230

231



233

234

235 Figure 4 geocoded interferogram 2004/04/06 – 2006/05/07. One fringe corresponds to 2.8 cm of displacement in Line of
 236 sight. The position of the fault trace at the surface estimated from post-seismic deformation is shown.

237

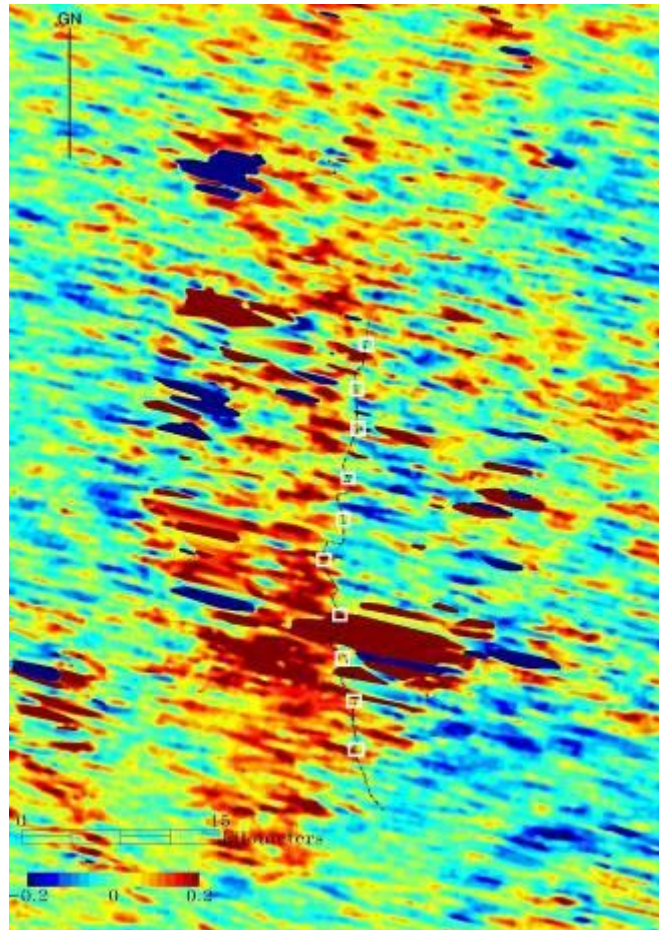
238 Although the precision of image correlation applied to the radar amplitude images (with a slant range
 239 resolution of about 7 m) is much poorer than with interferometry, we tested the methodology in order to
 240 obtain an estimate of the deformation profile along the fault trace. This information could complement the
 241 radar interferometry information where surface displacement is too high (i.e. close to the rupture). Figures 5
 242 and 6 show the results (offset image and deformation profile) of the correlation. The displacement values on
 243 the rupture are determined from linear least square fit to displacement profiles drawn perpendicularly to the
 244 rupture. Based on the a priori knowledge of the fault position, this procedure (Avouac et al., 2006; Leprince
 245 et al., 2007) fits the deformation profile perpendicularly to the fault by 2 half straight lines on either side of the
 246 fault (the profiles are limited by the same point on the fault); the deformation estimate is then provided by the
 247 difference between the two fitted values at the fault point location.

248 The observed displacement ranges from 1.5 to 2 m (consistent with Fenton & Bommer (2006) if we assume
249 that in view of the geometries of the fault (dip $>70^\circ$) and the sensor (incidence ~ 2 , we are mainly
250 measuring vertical deformation) in the southern part of the rupture and 0.7 m to 1.3 in the northern section
251 (consistent with Hasimoto et al. (2007) who proposed a smaller displacement on the northern segment).
252 Azimuth offsets were not used as they are not relevant to our study. Because the deformation is mainly
253 oriented east-west, there are no measurable offsets in the azimuth direction (\sim south-north displacements)
254 taking into account the sensitivity of this technique if applied on ENVISAT ASAR data ($1/10^{\text{th}}$ of the pixel
255 size, i.e. ~ 40 cm).
256

257

258

259



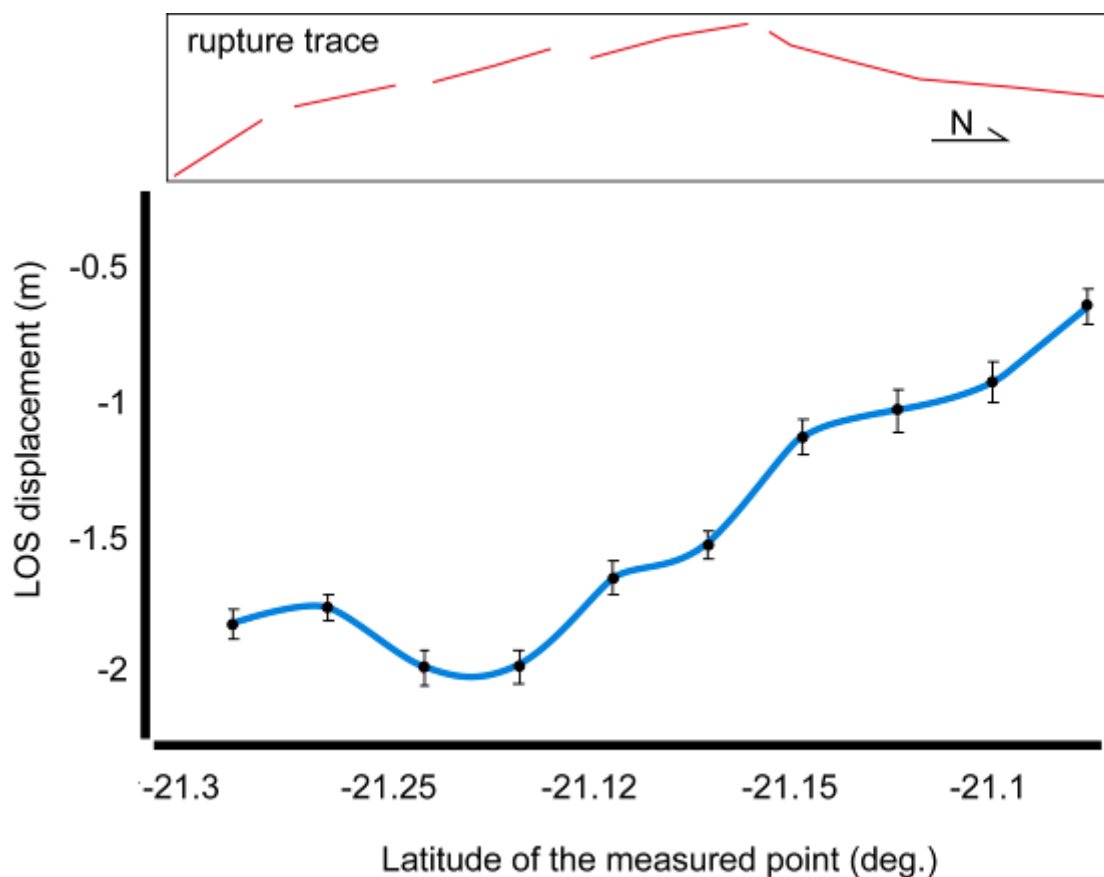
260

261

262 Figure 5: Slant range offset (in pixels of about 7 m) between images 2004/04/06 and 2006/05/07. The location of the
263 rupture trace is shown. Squares indicate the location of the points on Figure 6, where offsets have been estimated.

264 Although the result is noisy, the position of the rupture is consistent with the derived displacement variation.

265



267

268

269 Figure 6: LOS displacement on the fault (in metres, east side with respect to west side) versus latitude obtained using
 270 the cosi-corr (Leprince and Ayoub, 2007) profile/stacking tool. The error bars correspond to the standard deviation in the
 271 linear regressions to either side of the fault.

272

273 5 Co-seismic deformation modelling

274

275 We propose an inversion based on an elastic dislocation model (Okada, 1985; Briole, 1986). Because of the
 276 large number of parameters (location, dip, depth, size, displacement for the two fault segments) to be
 277 inverted using only one component (Line of sight) of the deformation, we had to use pre-existing information
 278 (estimates of the parameters from Feitio, 2008) and trial-and-error adjustments to correct several of the
 279 parameters before inverting the slip values. For convenience, we used rake values of -90° for both segments
 280 (Feitio, 2008, used -80°).

281 As in Hasimoto et al., (2007) we propose a model with two contiguous fault segments implied in the
 282 deformation. However, the position and orientation of the segments are derived from the trace obtained from

283 the post-seismic deformation. Thus, the orientation of the northern segment differs from that proposed by
 284 Hasimoto et al., (2007).

285 Table 5 summarizes the resulting parameters. The slip values are consistent with Hasimoto et al., (2007).

286

287 Table 5: Inverted model parameters.

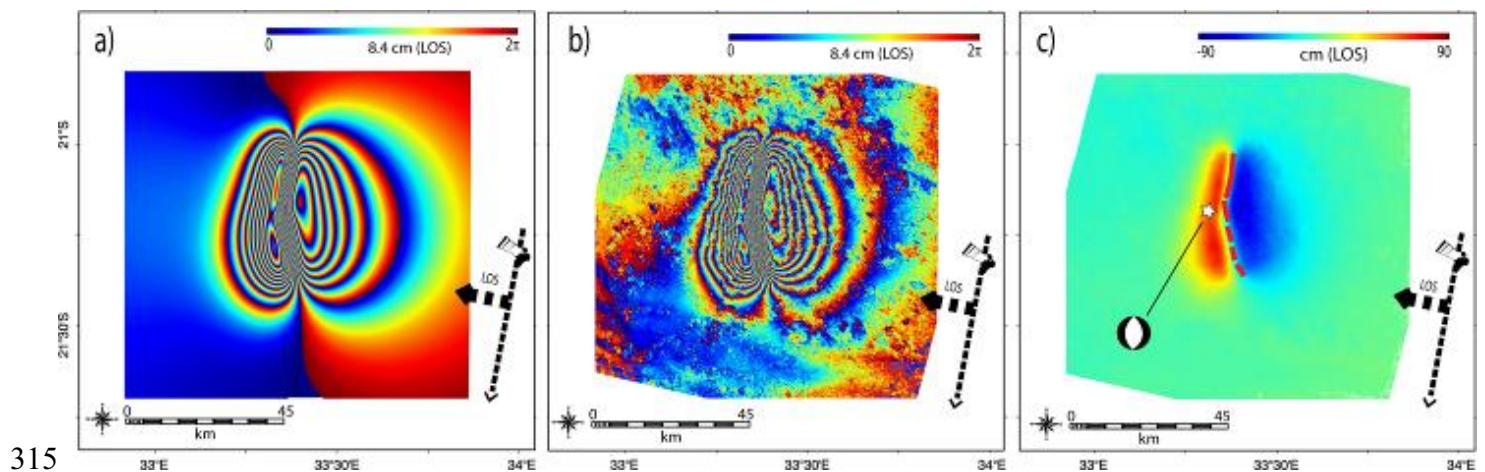
288

<i>Parameter</i>	<i>Southern segment</i>	<i>Northern segment</i>
UTM 36 S east (km) of the centre of the segment	537	537
UTM 36 S north (km) of the centre of the segment	7647	7667
Segment azimuth (deg)	170	-172
Depth of the top of the segment (km)	5	3
Half length of the segment (km)	10	10
Width of the segment (km)	11	9
Dip (deg)	70	70
Slip (mm)	3400	2660

289

290 As described in section 3, the model obtained is suitable for inclusion in a procedure for improving the
 291 unwrapping process and interpolating where the interferogram's coherence is inadequate. Figure 7 shows
 292 the modified interferogram. We should state that improvement can be expected to be better in the far-field
 293 deformation areas (where the model is more reliable, being derived from interferometric data unavailable in
 294 the rupture zone). Near the rupture, the result still appears underestimated. For instance, the maximum
 295 relative deformation is about 115 cm in LOS (i.e., about 125 cm in vertical) as opposed to 2 m observed by
 296 Fenton & Bommer (2006) and Figure 7. However, the underestimation is much less than with a direct
 297 unwrapping of the interferogram. We think that such interferogram unwrapping (once the area along the
 298 rupture has been masked) could be used for inverting a more complex deformation model provided it was
 299 combined with additional data. As only one component of deformation is available, if we intend to consider
 300 inhomogeneous slips on the fault planes, we would need additional information in order to cope with the
 301 non-uniqueness of the solution, in particular other components of deformation and a better description of

302 fault geometry. In fact, in the case of our simple model based on constant slip on two large surfaces
 303 combined with basic assumptions on the geometry, we do not believe that re-using these results to improve
 304 the model could provide better results than those based on data derived from displacement data obtained by
 305 fringe digitizing. To test such a possible “iterative” method (improve the previous model using the corrected
 306 interferograms), at least two components of deformation would be required. In the present test case, the
 307 available data set does not allow us to go further. Let us note that an additional advantage for such
 308 interferogram improvement would be to facilitate interferogram stacking. Indeed, if we had several
 309 interferograms for the same event, we would plan to average them in order to reduce noise or atmosphere
 310 or compensate for residual biases (not fully compensated). For such stacking procedures, prior unwrapping
 311 is needed. Because of the limitations of standard unwrapping with a high deformation gradient and areas of
 312 low coherence, such stacking could fail. In this perspective, the described procedure could prove helpful, but
 313 unfortunately in our test case only one reliable interferogram was actually produced.
 314



315
 316
 317 Figure 7: a) Interferogram simulation obtained using the inverted parameters. One fringe corresponds to 8.4 cm in LOS.
 318 The approximate locations of the modelled fault surfaces are shown. b) Interferogram 2004/04/06 – 2006/05/07
 319 unwrapped taking into account the simulation and rewrapped for visualisation purposes (one fringe corresponds to 8.4
 320 cm in LOS) c) Interferogram 2004/04/06 – 2006/05/07 geocoded and unwrapped taking into account the simulation.
 321 Values in rad. The fault trace derived from post-seismic deformation is shown.

324 **8 Discussion and Conclusion**

325 The results presented in this paper provide new information for understanding surface displacement of the
326 Machaze earthquake in a broad sense.

327 We have used Satellite-based Radar Interferometry to map surface displacement during three phases (inter,
328 co and post-seismic) of the seismic cycle associated with the 2006 Machaze earthquake. The area affected
329 by the Machaze earthquake is not instrumented on the ground and it is only partially accessible in the field
330 due to the presence of land mines. This makes satellite remote sensing techniques the only tools available
331 to make broad-scale measurements in the area allowing the whole earthquake-induced surface
332 displacement to be observed. We have made use of archive data from both L-band and C-band sensors on
333 board J-ERS, ALOS-PALSAR and ENVISAT-ASAR respectively. The use of J-ERS data drawn from
334 archives to try to enhance possible inter-seismic surface displacements is an interesting aspect of the InSAR
335 technique for such *a posteriori* studies.

336 As the surface displacement characteristics during the three phases of the seismic cycle differ in terms of
337 linearity, deformations gradients and localization, we adapted *ad hoc* processing strategies to the data
338 appertaining to each observation period. In particular, our study started by identifying the location of a
339 candidate surface rupture based on the post-seismic surface displacement location, which completes and
340 complements the surface rupture field observations made by Fenton & Bommer (2006). Interferogram
341 stacking (by averaging) was needed for inter- and post-seismic regimes, while for the co-seismic phase we
342 proceeded by visual selection of reliable interferograms from an extensive interferogram series and used a
343 simulation (from an elastic dislocation model) for improving phase unwrapping. Finally, we proposed a new
344 inversion of the earthquake parameters taking into account the identified rupture location.

345 The post-seismic deformation seems to be constant with time, about 3.5 cm/year for at least the two years
346 after the earthquake. Such a post-seismic phenomenon is intriguing and begs further dedicated
347 investigation. As far as this study is concerned, we tried to discriminate broadly among different possible
348 known source phenomena such as viscoelastic relaxation (e.g. Thatcher, 1983; Freed et al., 2007),
349 poroelastic rebound (e.g. Jonsson et al., 2003), afterslip (e.g. Marone et al., 1991) and dilatancy recovery
350 (e.g. Fielding et al., 2009). Although these phenomena might have occurred, we could reasonably rule out
351 substantial contribution from viscoelastic relaxation and poroelastic rebound, as these phenomena would
352 yield a post-seismic signal opposite in direction to the co-seismic signal, which was not the case here. The
353 dilatancy recovery phenomenon was observed geodetically on the BAM strike-slip fault system in Iran
354 (Fielding et al., 2009). Although this phenomenon is not well understood for normal faulting and certainly

355 would deserve more attention for the Machaze case, we might argue that dilatancy recovery would affect a
356 broad zone in the fault area, one not particularly limited by the fault plane, which is not our case. Afterslip
357 occurs when coseismic stress changes drive best candidate in the Machaze area, as its direction the same
358 as that of the coseismic slip, a fact observed elsewhere (e.g. Freed, 2007).

359

360 In further work, we intend to address the following issues about this earthquake that deserve investigation.

361 The post-seismic deformation over a longer period has to be monitored with the objective of detecting
362 deformation slowing (or termination) in order to be able to model for this evolution.

363 Finally, the deformation observed north-north-west of the epicentre after the earthquake is still unexplained
364 and should be investigated.

365

366 **9 Acknowledgements**

367

368 The study was conducted with the support of the Research Division of BRGM. Parts of the presented study
were carried out in the framework of the MSc work of B. Ristori presented at Ecole Sup. des Géomètres
et Topographes in June 2009. We wish to thank the reviewers for their help in improving the manuscript.

371

372 **10 References**

373

374 Avouac, J.P., Ayoub, F., Leprince, S., Konca, O., & Helmberger, D.V. (2006), The 2005, Mw 7.6 Kashmir
375 earthquake: Sub-pixel correlation of ASTER images and seismic waveforms analysis, *EPSL*, 249, 514-528.

376

377 Briole, P., De Natale, G., Gaulon, R., Pingue, F., & Scarpa, R. (1986), Inversion of geodetic data and
378 seismicity associated with the Friuli earthquake sequence (1976-1977) Italy, *Annales Geophysicae*, 4 B,
379 481-492

380

381 Feitio P. (2008), Relocation of the Machaze and Lacerda earthquakes in Mozambique and the rupture
382 process of the 2006 Mw 7.0 Machaze earthquake, Master Paper, IISEE, Tsubuka, Japon,
383 (<http://iisee.kenken.go.jp>)

384

385 Fenton C. & Bommer J., (2006), The M_w 7 Machaze, Mozambique, Earthquake of 23 February 2006,
386 *Seismological Research Letters*, 77, 426-432
387

388 Fielding, E.J., Lundgren, P.R., Bürgmann, R., Funning, G.J., (2009), Shallow fault-zone dilatancy recovery
389 after the 2003 Bam earthquake in Iran, *Nature*, 458, 64-68
390

391 Freed, A.M., (2007), Afterslip (and only afterslip) following the 2004 Parkfield, California, earthquake,
392 *Geophysical Research Letters*, 34, art. no. L06312
393

394 Gamma RS, (2008), "IPTA Reference Manual", Gamma RS, Gumligen
395

396 Hashimoto M., Fukushima Y. & Ozawa T. (2007), co-seismic and post-seismic displacements from the
397 Mozambique earthquake of 22 February 2006 detected by InSAR, *Fringe07*, Frascati, Italy, 26th-30th
398 November 2007
399

400 Jónsson, S., Segall, P., Pedersen, R., Björnsson, G., (2003), *Post-earthquake ground movements correlated*
401 *to pore-pressure transients*, *Nature*, 424 (6945), 179-183
402

403 Le Mouélic S., Raucoules D., Carnec C. & King C., (2005), A Least-squares adjustment of multi-temporal
404 InSAR data – Application to the ground deformation of Paris, *Photogrammetric Engineering and Remote*
405 *Sensing*, 2, 197-204
406

407 Leprince S. & Ayoub F., (2007), Cor-registration of Optically Sensed Images and Correlation, *User's Guide to*
408 *COSI-CORR*, California Institute of Technology, Pasadena
409

410 Leprince S., Ayoub F., Klinger Y. & Avouac J.P., (2007), Co-Registration of Optically Sensed Images and
411 Correlation (COSI-Corr): an Operational Methodology for Ground Deformation Measurements, IGARSS
412 2007, 23-27 July 2007 - Barcelona, Spain

413 L3pez-Querol, S., M. Coop, W.W. Sim, J.J. Bommer & C. Fenton, (2007), Back-analysis of liquefaction in
414 the 2006 Mozambique earthquake. *Georisk* 1(2), 89-101.
415

416 Marone, C.J., Scholtz, C.H., Bilham, R., (1991), On the mechanics of earthquake afterslip, *Journal of*
417 *Geophysical Research*, 96 (B5), 8441-8452
418

419 Massonnet, D. & Feigl, K.L., (1998), Radar interferometry and its application to changes in the earth's
420 surface, *Reviews of Geophysics*, 4, 441-500.
421

422 Michel R. & Avouac J., (2002), Deformation due to the 17 August 1999 Izmit, Turkey, earthquake measured
423 from SPOT images. *Journal of Geophysical Research B: Solid Earth*, 4, 2-1.
424

425 Okada, Y.,(1985), Surface deformation due to shear and tensile faults in a Halfspace, *Bull. Seismol. Soc.*
426 *Amer.*, 75, 1135–1154
427

428 Raucoules D., Colesanti C. & Carnec C., (2007), Use of SAR interferometry for detecting and assessing
429 ground subsidence, *Compte Rendus Geosciences*, 5, 289-302
430

431 Thatcher, W., (1983), Nonlinear strain buildup and the earthquake cycle on the San Andreas fault. *Journal of*
432 *Geophysical Research*, 88 (B7), 5893-5902
433

434 Wegmuller, U., Werner, C. & Strozzi, T., (1998), SAR interferometric and differential interferometric
435 processing chain. *International Geoscience and Remote Sensing Symposium (IGARSS)*, 2, 1106-1108, July
436 1998, Seattle
437

Figure 1
[Click here to download high resolution image](#)

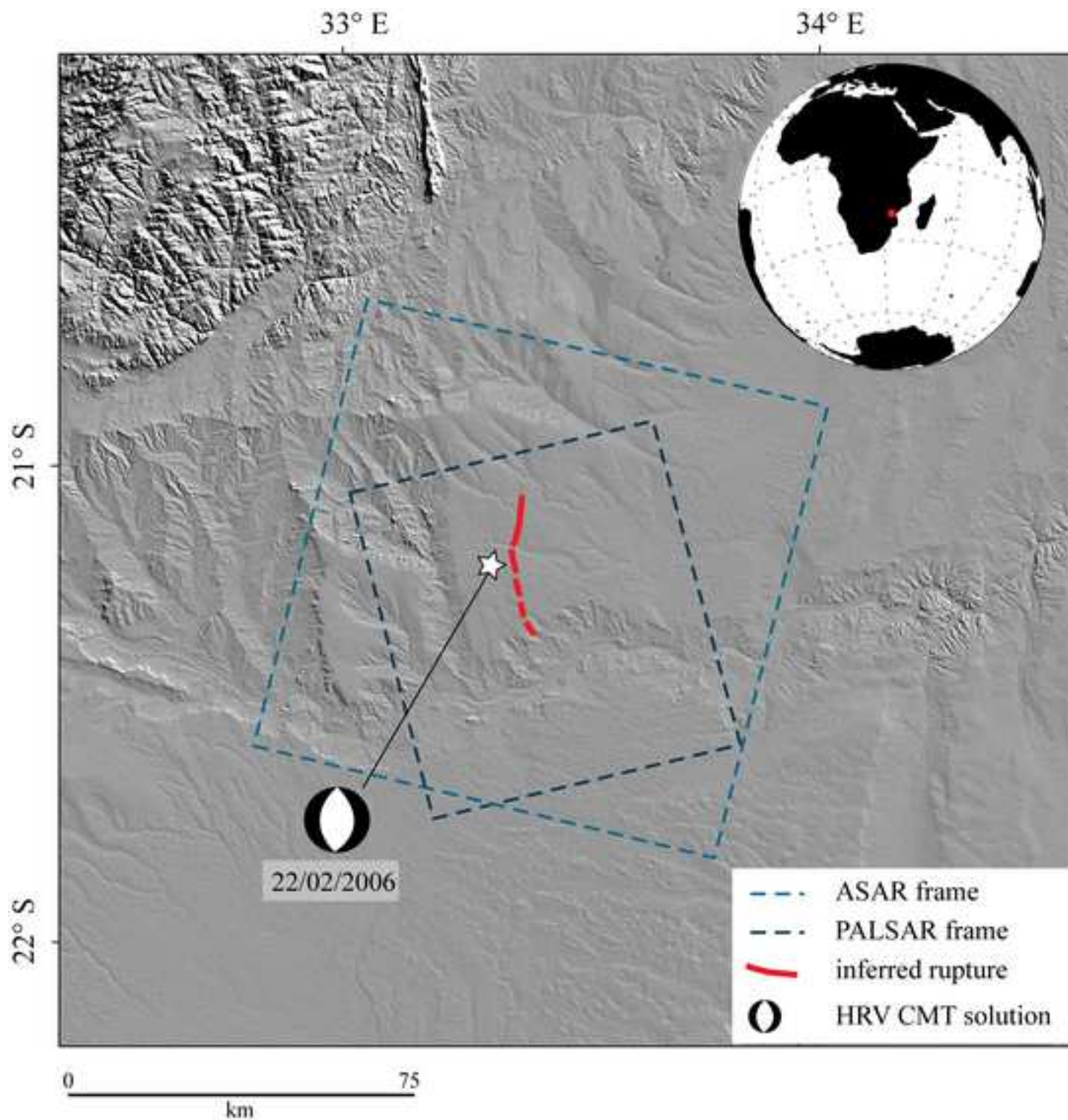


Figure 2
[Click here to download high resolution image](#)

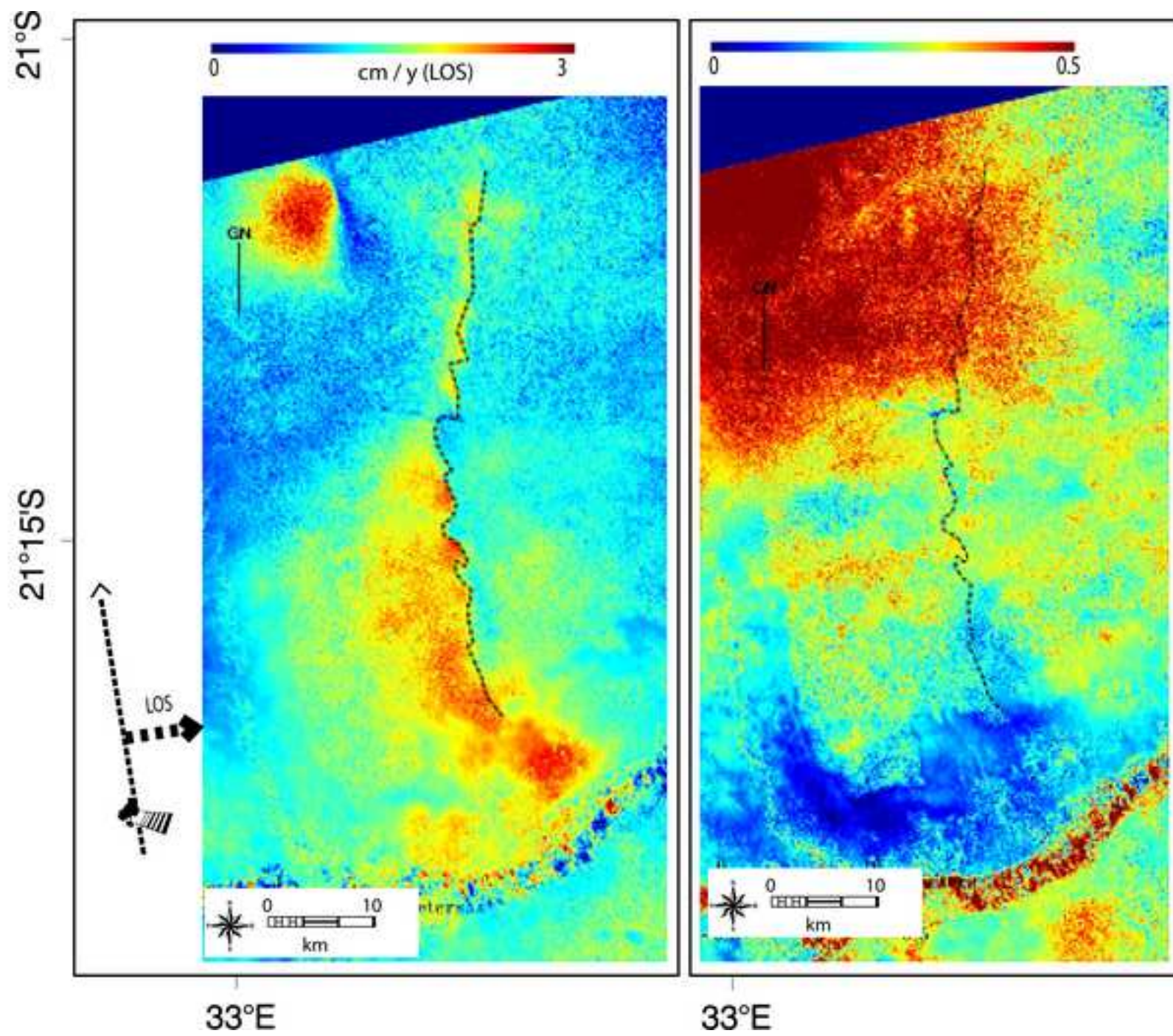


Figure 3
[Click here to download high resolution image](#)

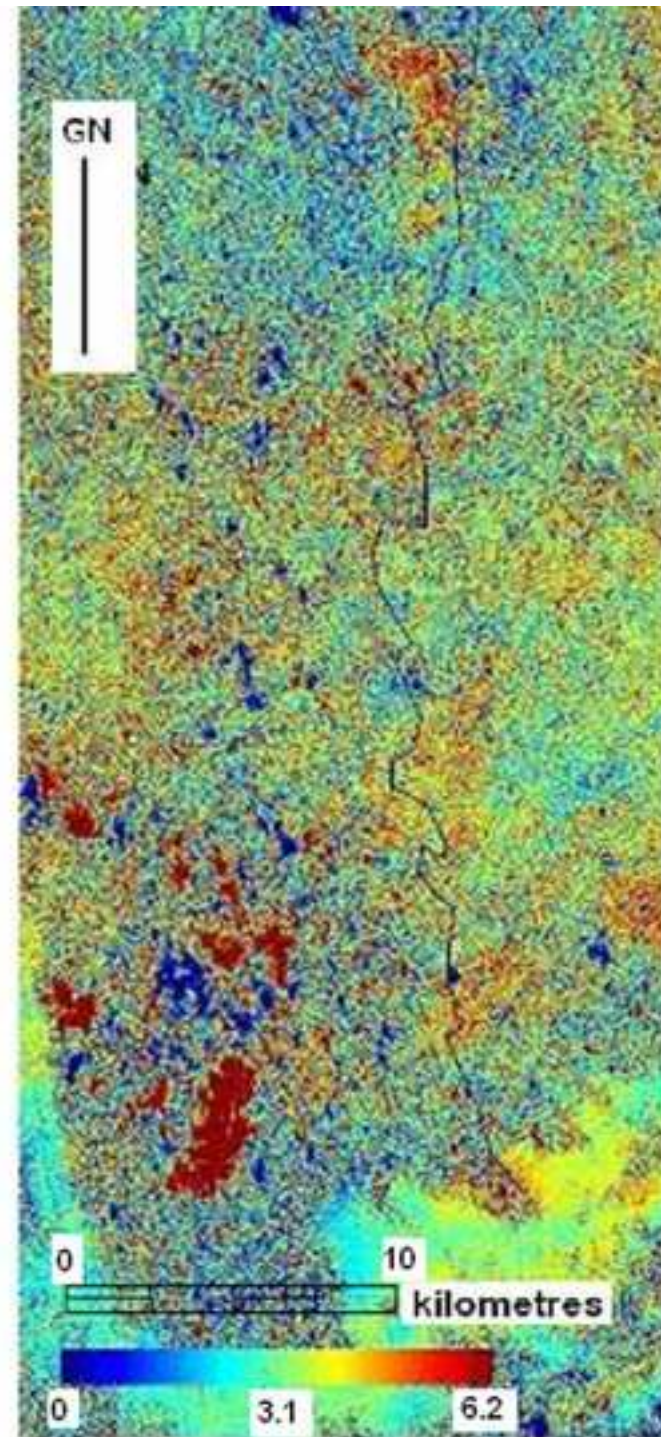
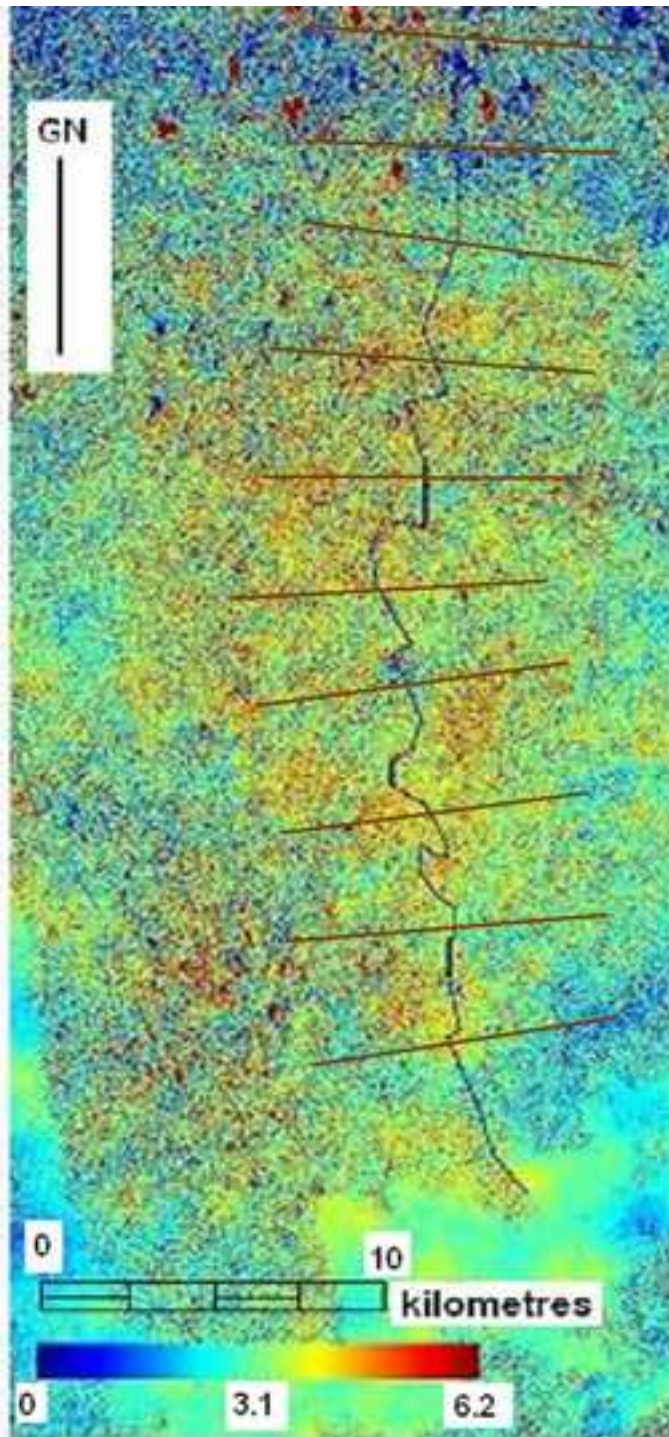


Figure 4
[Click here to download high resolution image](#)

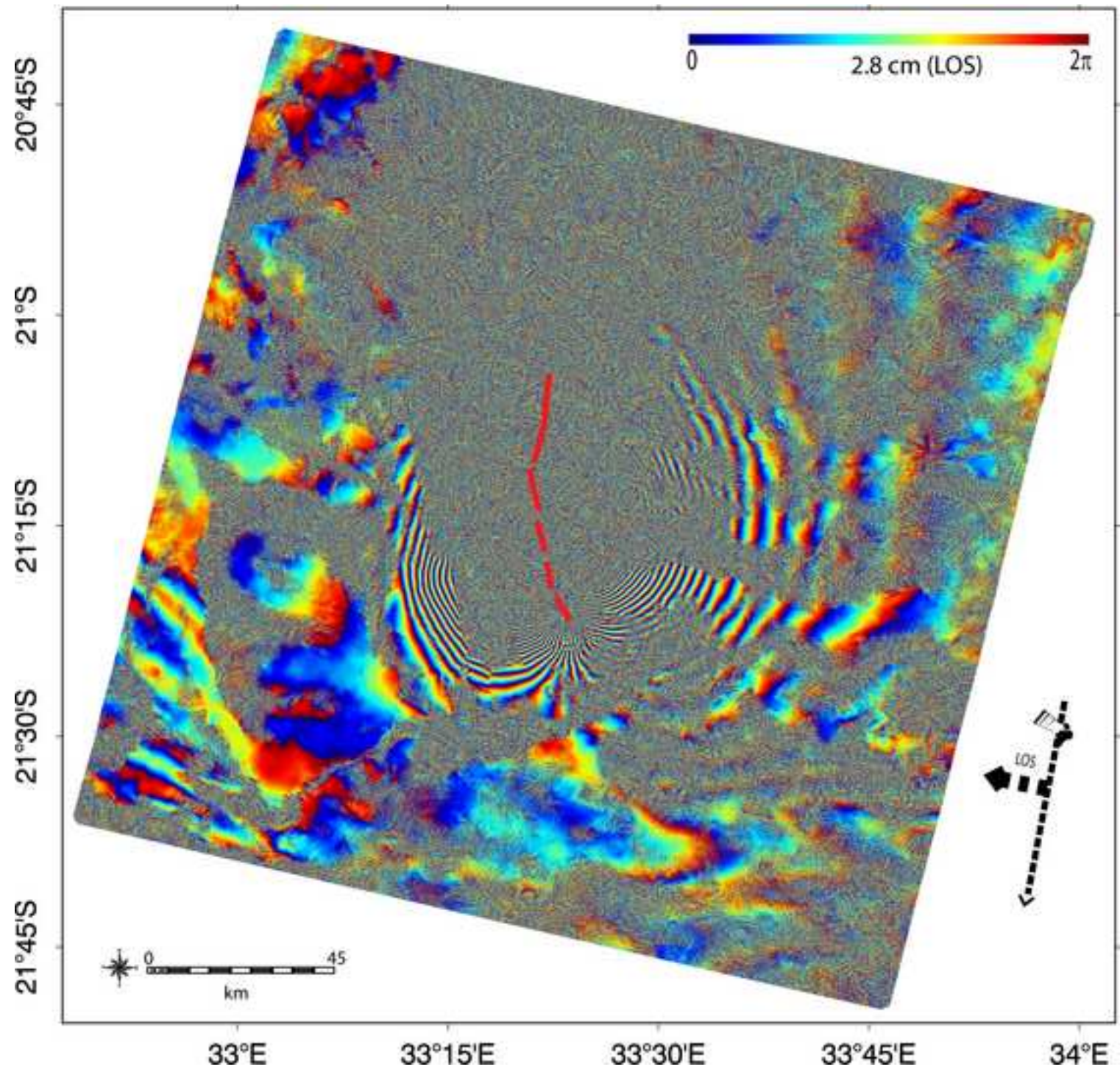


Figure 5
[Click here to download high resolution image](#)

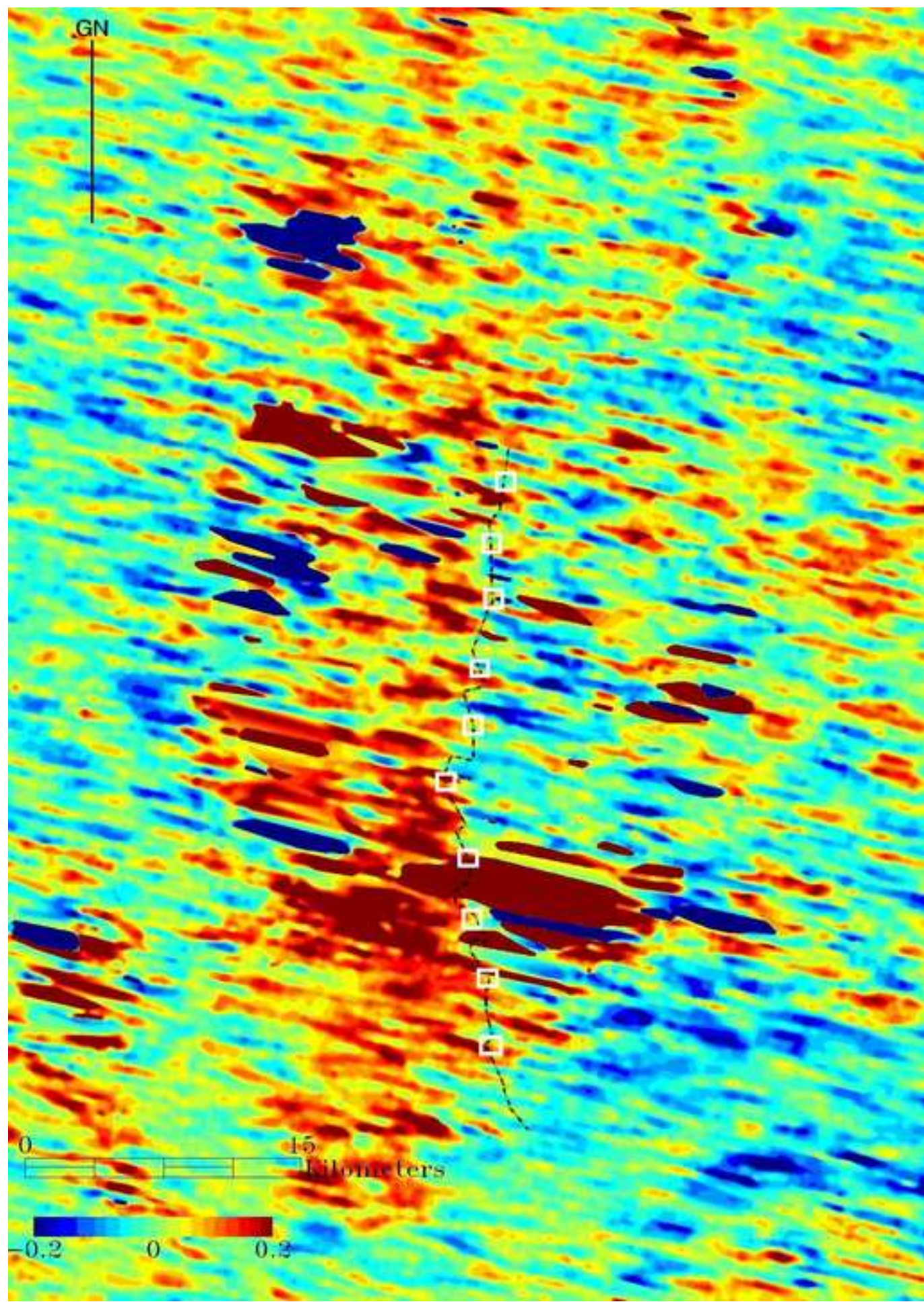


Figure 6
[Click here to download high resolution image](#)

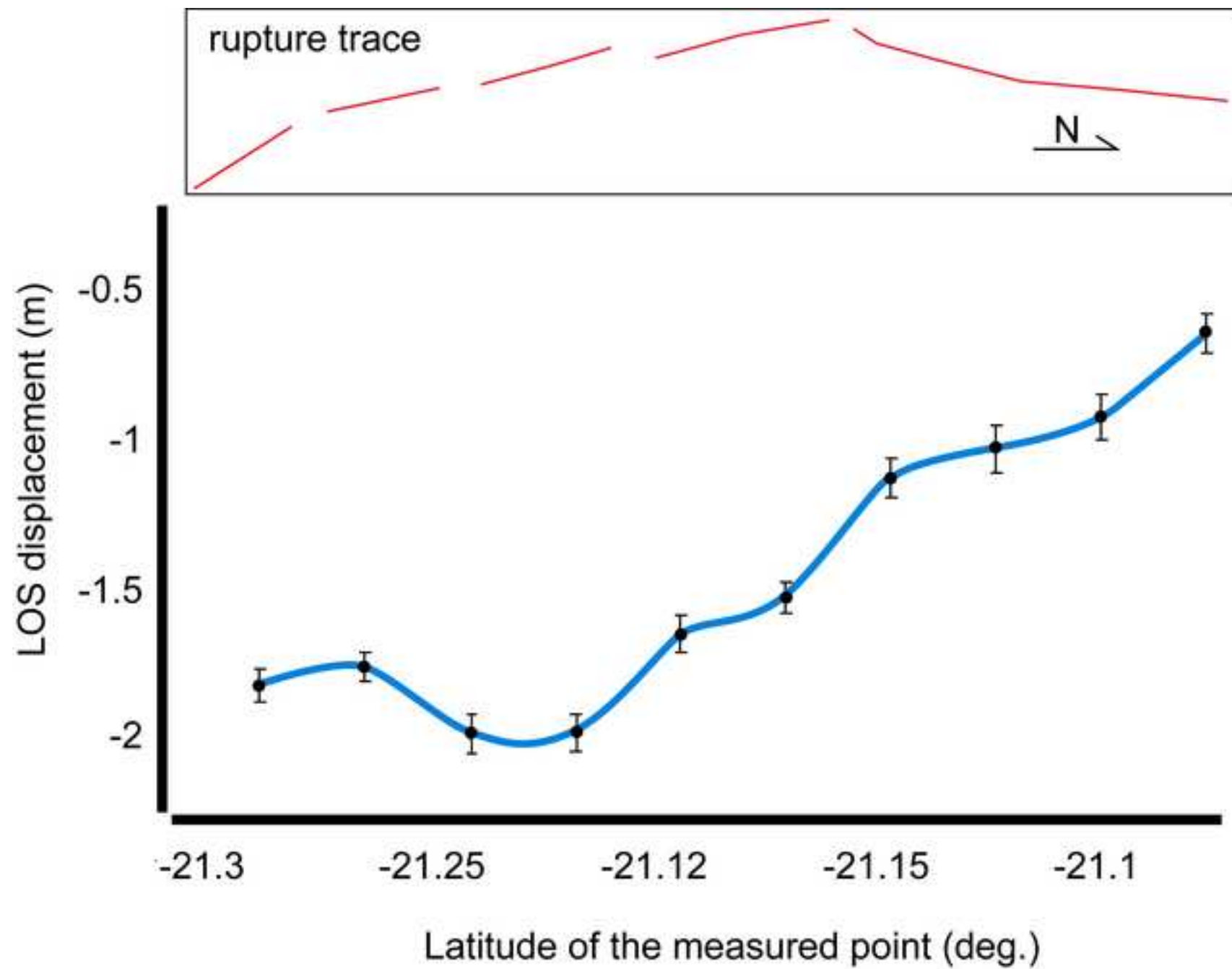


Figure 7
[Click here to download high resolution image](#)

